

Entanglement phases and phase transitions in the monitored free fermion systems of localization

Yu-Jun Zhao,^{1,2} Xuyang Huang,² Yi-Rui Zhang,² Han-Ze Li,^{2,3,*} and Jian-Xin Zhong^{2,1,†}

¹*School of Physics and Optoelectronics, Xiangtan University, Xiangtan 411105, China*

²*Institute for Quantum Science and Technology, Shanghai University, Shanghai 200444, China*

³*Department of Physics, National University of Singapore, Singapore 117542*

The interplay between quantum measurement and localization significantly alters the spreading of quantum information. In this work, we investigate monitored free-fermion chains with localized potentials. With the aid of the quantum trajectory method and finite size analysis, we numerically reveal that the Berezinskii–Kosterlitz–Thouless transition, which emerges in monitored free-fermion chains, is robust in the presence of localization. To understand this, we construct a phase diagram that diverges at a boundary described by entanglement propagation. We find that the monitored system with Stark-localized decays quickly under small measurement strength, whereas the Anderson-localized system decays more slowly. By incorporating localization effects, this work advances our understanding of how measurement competes with the coherent spreading of quantum information. Our findings can potentially be realized in cold atom systems, trapped ions, and quantum dot arrays.

I. INTRODUCTION

Classical paradigms of nonequilibrium quantum physics—such as thermalization under the eigenstate thermalization hypothesis [1–5] and its counterpoint in the quantum Zeno effect [6–10], offer a striking tension: while coherent dynamics generically scramble information and build volume-law entanglement, frequent observations can freeze evolution by continually projecting local degrees of freedom. This tension naturally leads to the notion of a measurement-driven reorganization of quantum states: as the rate or strength of monitoring is increased, the balance between entanglement production and removal can qualitatively change, suggesting a sharp transition in the long-time entanglement structure. This phenomenon is now understood as a measurement-induced phase transition (MIPT) [11–18], in which entanglement scaling morphs from volume law to area law due to the backaction of measurements.

A broad body of work has established both the ubiquity and diversity of MIPTs across platforms and protocols [19–66]. In random quantum circuits [37–51], interleaving unitary gates with stochastic measurements yields a finite-threshold transition. Related transitions appear under Hamiltonian dynamics with projective or continuous monitoring [52–56], and persist for both projective and indirect measurements. Across these settings, the steady-state phases (volume, logarithmic/sub-volume, and area) and their critical properties depend on symmetries [20, 49, 59, 60], dimensionality [61], and the microscopic structure of measurements [38, 62–66], revealing a rich taxonomy of measurement-driven universality classes.

In the presence of localization, the landscape becomes more intricate. The root cause lies in the fact that localization tends to confine particles or quantum information to local regions, thereby significantly suppressing the generation and propagation of long-range entanglement. Different types of localization affect entanglement and information spreading through

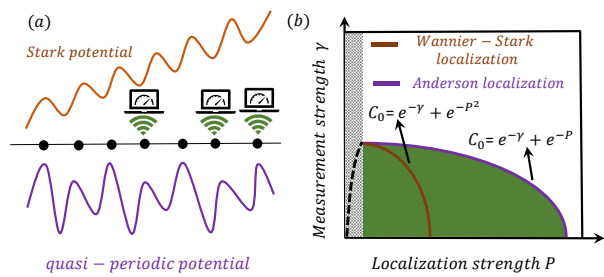


FIG. 1. (a): Monitored half-filled fermions in SP (brown) and QPP (purple). (b): The phase boundaries in the phase diagram are formed by different localization mechanisms (Wannier–Stark localization and Anderson localization). We present the general solution form, with specific parameters given below. The grey region corresponds to the case of a very weak localization potential, where we tend to revert to the results obtained from the Keldysh field theory [61]; the black dashed line corresponds to the phase boundary within this region.

their respective physical mechanisms, and may thus alter the stability of phases and critical behavior in different ways. For example, disorder or quasi-periodic potential (QPP) induced Anderson localization and Stark potential (SP) induced Stark localization [67–69] imprint distinct single-particle spectra, spatial profiles and transport properties that can [70–91], in principle, reshape measurement-driven entanglement phases and transitions.

Previous studies in disordered [57] and quasi-periodic systems [58] have revealed the characteristics of measurement-induced phase transitions, with their results mainly emphasizing the persistence of the BKT universality class and the regulation of phase laws by Anderson localization potentials. In contrast to these studies based on Anderson localization, we choose the Stark localization system as a stronger localization platform, taking this as an opportunity to further explore the competition between measurement and different localization mechanisms, and attempt to construct a phase diagram that diverges at a boundary characterized by entanglement propa-

* hanzeli@u.nus.edu

† jxzhong@shu.edu.cn

gation under distinct localization mechanisms.

Against this backdrop, we ask two connected questions at the intersection of measurement and localization: (I) Will a change in the localization mechanism alter the critical universality class of the MIPT phase diagram, or do the two cases follow the same critical laws? (II) Is it possible to establish a unified phase diagram to characterize entanglement phase transitions arising from the interplay between different localization mechanisms and measurements? Addressing these questions disentangles universal from non-universal ingredients in the measurement-localization competition and yields operational criteria for experimental tests across platforms ranging from cold atomic systems [52–54, 92–94] and trapped ions [95, 96] to quantum dot arrays [97].

To address question (I), we employ a one-dimensional free-fermion system as our platform. Under both a SP (realizing Stark localization) and a QPP (realizing Anderson localization), we introduce random projective measurements with tunable strength. By analyzing the system's steady-state entanglement entropy and effective central charge, we investigate the impact of the measurement-localization coupling on the entanglement phase transition. For question (II), we identify the physical mechanisms that play a central role in the entanglement phase transition, thereby formulating a universal statement concerning different localization mechanisms. Furthermore, we obtain several physical pictures, which are summarized schematically in Fig. 1.

The remainder of this paper is organized as follows. In Sec. II, we introduce the tight-binding model in the presence of a localization potential and outline the quantum trajectory method used to simulate continuous measurement dynamics. In Sec. III, we present our understanding of the phase boundary arising from the interplay between different localization mechanisms and measurements, together with the entanglement phase diagram of MIPTs and the semi-analytical phase boundary we obtain. We then investigate the central charge, connected correlation function, and critical universality classes under both SP and QPP. Finally, Sec. IV summarizes the entire work.

II. MODEL AND METHOD

We consider a spinless one-dimensional fermions model of localization, subject to continuous measurements:

$$H = -J \sum_j (c_j^\dagger c_{j+1} + \text{h.c.}) + \sum_j P_j n_j, \quad (1)$$

where P_j represents the strength of potential at lattice site j :

$$P_j = \begin{cases} \Delta j / L, & \text{SP}, \\ V \cos\left(\frac{2\pi j}{\tau} + \theta\right), & \text{QPP}, \\ \varepsilon_j, & \text{Anderson disorder}, \end{cases} \quad (2)$$

with $J = 1$ is the strength of the nearest-neighbor hopping term, c_j and c_j^\dagger are the annihilation and creation operators

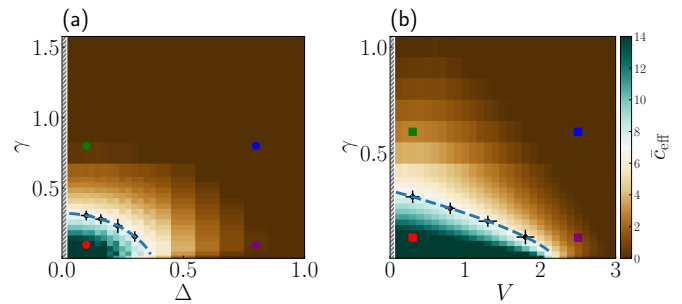


FIG. 2. Phase diagrams and phase boundaries extracted from the effective central charge. (a) Phase diagram under joint tuning of the measurement strength and SP strength; (b) Phase diagram under joint tuning of the measurement strength and the QPP strength. Colors indicate the effective central charge \bar{c}_{eff} , extracted from the finite-size scaling of half-chain entanglement entropy: green corresponds to large \bar{c}_{eff} values (log-law-like regime), while brown corresponds to $\bar{c}_{\text{eff}} \rightarrow 0$ (area-law regime). Dashed curves denote the semi-analytical expressions for phase boundaries derived by Eq. (12). Black solid dots mark four phase transition points obtained through finite-size scaling analysis and data collapse. The grey region corresponds to the case of a very weak localization potential, where we tend to revert to the results obtained from the Keldysh field theory [61]; therefore, it is not shown in the diagram. In the subsequent finite-size scaling analysis, four representative points on each phase diagram (marked in red, green, blue, and purple, respectively) are selected to characterize the entanglement scaling behavior at the phase boundary of that point.

of the spinless fermion at site j . Here, Δ denotes the SP strength, L is the number of lattice sites in the system, and the parameters V , τ , and θ represent, respectively, the QPP strength, the golden mean $(\sqrt{5} + 1)/2$, and the phase shift of the potential. The on-site potential ε_j is an independent random variable drawn from the uniform distribution $[-W, W]$, where W is the disorder strength. We initialize the system in a Néel state, that is, $\psi(t = 0) = \prod_{i=1}^{L/2} c_{2i-1}^\dagger |\text{vac}\rangle$, where $|\text{vac}\rangle$ is the vacuum state, and consider its evolution under open boundary conditions (OBCs). We perform continuous measurements uniformly on all lattice sites with a finite measurement rate γ , where quantum-jump events occur according to the standard quantum-jump trajectory formalism [98–101].

The corresponding stochastic Schrödinger equation is given by [54, 94, 102, 103]

$$\begin{aligned} d|\psi(t)\rangle = & -iH|\psi(t)\rangle dt \\ & + \sum_{j=1}^L \left[\frac{c_j^\dagger c_j |\psi(t)\rangle}{\sqrt{\langle\psi(t)|n_j|\psi(t)\rangle}} - |\psi(t)\rangle \right] dW_j(t), \end{aligned} \quad (3)$$

where $n_j = c_j^\dagger c_j$ is the local particle number operator being monitored. The stochastic variables $dW_j(t)$ take values 0 or 1 according to independent Poisson processes with mean $\langle\langle dW_j(t)\rangle\rangle = \gamma\langle n_j \rangle dt$, and $\langle\langle \dots \rangle\rangle$ denotes the noise average. In this formulation, the Born probabilities are encoded in the normalization factor $\sqrt{\langle\psi(t)|n_j|\psi(t)\rangle}$, which ensures that the probability of each measurement outcome is consis-

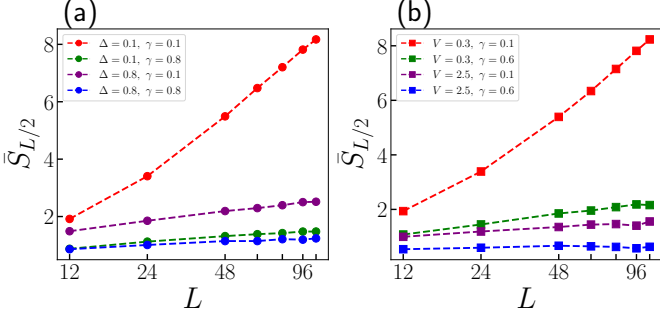


FIG. 3. Entanglement entropy versus system size for representative points. (a) Results corresponding to the four selected points from Fig. 1(a): $\Delta = 0.1, \gamma = 0.1$, $\Delta = 0.1, \gamma = 0.8$, $\Delta = 0.8, \gamma = 0.1$, and $\Delta = 0.8, \gamma = 0.8$; (b) Results corresponding to the four selected points from Fig. 1(b): $V = 0.3, \gamma = 0.1$, $V = 0.3, \gamma = 0.6$, $V = 2.5, \gamma = 0.1$, and $V = 2.5, \gamma = 0.6$. The plots show the half-chain entanglement entropy $\bar{S}_{L/2}$ as a function of system size L , revealing the scaling behavior under different potential and measurement strengths. Log-log axes are used throughout for visual clarity.

tent with quantum mechanics, while the Poisson increments $dW_j(t)$ determine whether a measurement event occurs at site j during each infinitesimal time step. As a result, the system evolves along many possible quantum trajectories starting from the same initial state, and statistical properties of observables are obtained by averaging over a large ensemble of such trajectories without any postselect. We use 500 independent trajectories in our numerical simulations. The main physical quantity that we address is entanglement entropy. Divide the system into two subsystems A and B , which have sizes ℓ and $L - \ell$ ($\ell \leq L/2$), respectively (L represents the system size). Then, the entanglement entropy is defined as:

$$S = -\text{Tr}(\rho_A \log \rho_A), \quad (4)$$

where ρ_A is the reduced density matrix of the subsystem A for a given wave function $|\psi\rangle$, that is, $\rho_A = \text{Tr}_B(|\psi\rangle\langle\psi|)$, where Tr_B is the partial trace with respect to the part B . S is initially 0 and increases over time, reaching a saturated value in the long-time limit. We calculate the long-time steady-state entanglement entropy for each trajectory, take their average, and finally obtain \bar{S} .

III. RESULTS

A. Phase boundaries

As stated in Sec. II, in the specific study, we divide the system into two subsystems, A and B , in order to calculate the entanglement entropy. Consider such a bipartite system governed by purely quantum dynamics, the growth rate of its entanglement entropy takes the following form [39, 104–107]:

$$\dot{S}_\ell = -i \|H_{AB}\| \lambda(\rho), \quad (5)$$

$$\lambda(\rho) := \text{Tr}(h_{AB} [\rho, \rho_A \otimes \mathbf{I}_B]), \quad (6)$$

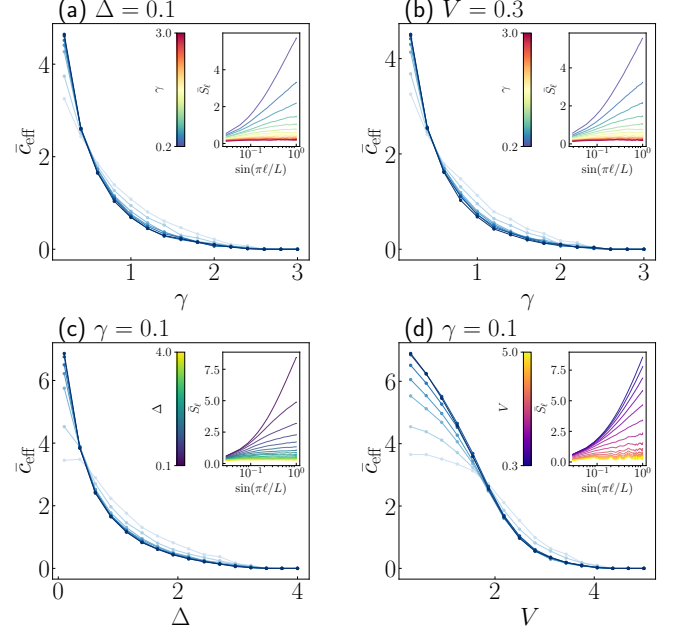


FIG. 4. Effective central charge \bar{c}_{eff} versus various control parameters with entanglement scaling insets. (a) Fixed $\Delta = 0.1$, varying measurement strength ; (b) fixed $V = 0.3$, varying measurement strength ; (c) fixed $\gamma = 0.1$, varying SP strength ; (d) fixed $\gamma = 0.1$, varying QPP strength. Insets display entanglement entropy versus $\sin(\pi\ell/L)$ on a logarithmic x -axis to emphasize scaling behavior. Shades of blue from light to dark correspond to system sizes $L = 12, 24, 48, 64, 80, 96, 112$, the variation in system size is also reflected in the extent of the x -axis in the insets.

where $\rho = |\psi(t)\rangle\langle\psi(t)|$, $h_{AB} := H_{AB}/\|H_{AB}\|$ ($\|\cdot\|$ is the operator norm), and \mathbf{I}_B is the identity operator for subsystem B . The Hamiltonian H_{AB} denotes the boundary interaction between subsystems A and B [104] :

$$H_{AB} = \sum_{i \in A} \sum_{j \in B} h_{i,j}, \quad (7)$$

where $h_{i,j}$ is an interaction operator acting on sites i and j . Of interest is the case where $\ell = L/2$. In our study of a fermionic system without long-range interactions, the entanglement entropy growth rate is finite and takes a constant value, denoted as G_0 . Since measurements and localized potentials both act to disentangle the system, even when small, the original volume-law entanglement entropy growth $S \sim G_0 t$ is transformed, under their combined effect, into a logarithmic form $S \sim \log(t)$, and, upon further increase, crosses over to an area-law scaling $S \sim t^0$. In our study, the phase boundary corresponds to the critical line separating the log-law region from the area-law region. Therefore, we find that at the phase boundary the entanglement entropy growth follows $S \sim C_0 \log(t)$, representing the lower bound of the log-law region and the upper bound of the area-law region (see Appendix A), where C_0 is a small constant. Assuming that under the influence of measurements and localized potentials the initial entanglement growth rate is renormalized to

$\Gamma(\gamma, P)G_0$, then at criticality one can write:

$$\Gamma(\gamma) + \Gamma(P) \sim C_0, \quad (8)$$

$\Gamma(\gamma)$ represents the entanglement suppression rate induced by the measurement strength γ . It quantifies the degree to which entanglement growth is suppressed per unit time under continuous measurement interventions. When γ is sufficiently large, entanglement growth can be strongly inhibited or even fully halted. To analyze this process quantitatively, we decompose the system's evolution into individual quantum trajectories. Each trajectory corresponds to a specific measurement history, and the dynamics are governed by an effective non-Hermitian Hamiltonian [94]:

$$H_{\text{eff}} = H - i \frac{\gamma}{2} \sum_u \mathcal{L}_u^\dagger \mathcal{L}_u, \quad (9)$$

where H is the original Hermitian Hamiltonian, γ is the measurement rate, and \mathcal{L}_u is the Lindblad operator. The non-Hermitian [108–121] term captures the non-unitary dissipative effects introduced by measurements. Under this non-Hermitian evolution, Under the trajectory-weighted average, the initial entanglement-entropy growth rate of the system in the presence of measurements is renormalized to (please refer to Appendix A for details):

$$\Gamma(\gamma) \sim G_0 \exp(-\gamma). \quad (10)$$

As shown in Eq. (6), under purely unitary evolution, entanglement growth is driven by the boundary coupling between subsystems A and B . The entanglement growth rate is fundamentally determined by the Hamiltonian term H_{AB} that connects A and B . In the presence of a localized potential, the spatial localization of particle states significantly suppresses the boundary coupling between regions, leading to a pronounced reduction in the entanglement growth rate [122]. Corresponding to the distinct localization properties of the wave functions in the SP and the QPP systems, the entanglement growth rate is modified by the localized potentials as:

$$\Gamma(P) \sim \begin{cases} G_0 \exp(-\Delta^2), & \text{SP} \\ G_0 \exp(-V), & \text{QPP} \end{cases} \quad (11)$$

where G_0 is the reference growth rate in the absence of any potential, Δ is the SP strength. Based on Eq. (8) and the envelope function of the entanglement growth rate Eq. (10) and Eq. (11), the phase boundaries in the systems with SP or QPP can be written as:

$$C_0 = \begin{cases} \exp(-6\gamma^{3/2}) + \exp(-8\Delta^2), & \text{SP} \\ \exp(-6\gamma^{3/2}) + \exp(-V/2), & \text{QPP} \end{cases} \quad (12)$$

Eq.(12) provides a phenomenological envelope-function expression [74], and in the Anderson case [123], the measurement further introduces a super-exponential envelope that strongly suppresses the coefficient C_0 . To validate Eq. (12),

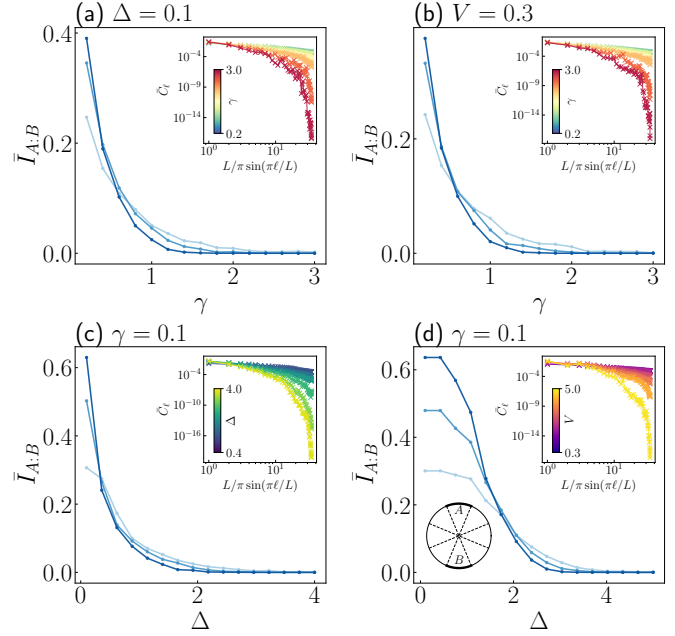


FIG. 5. Mutual information under varied control parameters, with scaling insets. (a) Fixed $\Delta = 0.1$, varying measurement strength γ ; (b) fixed potential strength $V = 0.3$, varying measurement strength γ ; (c) fixed measurement strength $\gamma = 0.1$, varying SP strength; (d) fixed $\gamma = 0.1$, varying QPP strength. Main panels show mutual information as a function of each parameter. Insets present correlation functions versus $\sin(\pi L/L)$, log-scaled on the x -axis to highlight scaling transitions. Shades of blue from light to dark correspond to system sizes $L = 12, 24, 48, 64, 80, 96, 112$, the variation in system size is also reflected in the extent of the x -axis in the insets.

we first map the effective central charge \bar{c}_{eff} over the parameter space spanned by the measurement strength γ and the localized potential strength (either Stark, Δ , or quasi-periodic, V), thereby characterizing the scaling regimes of the entanglement entropy. As shown in Fig. 2, the phase diagrams under varying measurement and potential strengths are presented for the SP and QPP systems. The colormap encodes \bar{c}_{eff} extracted from half-chain entanglement entropy; the horizontal axis is the measurement rate γ , and the vertical axis is the potential strength Δ or V . The diagrams clearly separate area-law and log-law regimes: regions with large \bar{c}_{eff} correspond to log-law growth (an entanglement-spreading phase), whereas regions with $\bar{c}_{\text{eff}} \approx 0$ exhibit suppressed entanglement. We find that increasing either the SP or QPP shrinks the entangled region and eventually eliminates the phase boundary, although the deformation is qualitatively different between SP and QPP. The dashed curves are fits to Eq. (12), which agree closely with critical points obtained via finite-size scaling (black dots). As the potential strength increases, the entangled region narrows, the boundary bends, and eventually terminates, reflecting the progressively stronger suppression of entanglement propagation caused by localization. Importantly, the boundary deforms differently in the two cases: for SP, it changes super-exponentially with Δ^2 ; for QPP, it

changes exponentially with V results that are fully consistent with the analytical structure established earlier. Together, they reveal a measurement-localization coupled entanglement phase transition: when the localization potential is small, the phase boundary is primarily determined by the measurement strength, and its descent is relatively gradual; as the localization potential increases, its suppression of entanglement growth causes the boundary to drop rapidly. However, because the Stark localization induced by SP is stronger than the Anderson localization induced by QPP, the phase boundary in Fig. 2(a) falls faster, reaching the area-law region much earlier. It is worth noting that, in the limit of vanishing localized potential $V(\Delta) = 0$, the system can be mapped onto a nonlinear σ model, in which no entanglement phase transition occurs [61]. In the limit $\gamma = 0$, in the thermodynamic limit, any finite strength of the SP or disorder (W) will lead to localization [70, 74, 123, 124], suppressing long-range information propagation, resulting in an area-law state, and no phase transition occurs in the system. However, due to finite-size effects, the localization length in this case exceeds the system size, which causes the $\gamma = 0$ region in Fig. 2(a) and Fig. 9 to still exhibit signatures of a phase transition. For the QPP, Anderson localization occurs only when $V > 2J$ [91], which is consistent with the results at $\gamma = 0$ in Fig. 2(b).

To further verify the scaling characteristics of different regions, we examine the dependence of the entanglement entropy \bar{S} on the system size L , selecting representative points (red, green, blue, purple) highlighted in Fig. 2. The corresponding results are shown in Fig. 3. It is evident that, under different measurement strengths and localization strengths, the dependence of \bar{S} on L exhibits significant differences. At the red-marked point in the phase diagram within the log-law region, \bar{S} shows a clear linear growth with $\log(L)$, indicating that the system is in a log-law-dominated phase. In this regime, the measurement rate and localized potential are insufficient to significantly disrupt the propagation of particles or information across the entire system, leading to logarithmic growth of entanglement. In contrast, in the area-law region (i.e., at non-red points), \bar{S} rapidly saturates to a constant as $\log(L)$ increases. This reflects the fact that, under strong measurement or strong localization, the propagation of quantum information is strongly suppressed, and entanglement can only be established within a finite range near the boundaries between adjacent regions, without extending throughout the system. This transition from a log-law to an area-law scaling reflects a measurement-and-localization driven entanglement phase transition: when the measurement or localization strength crosses a critical value, the system's information propagation capability undergoes a sudden change, leading to an abrupt shift in the scaling behavior of the entanglement entropy and the emergence of a well-defined critical boundary.

B. Phases and phase transitions

We next follow the finite-size flow of the effective central charge \bar{c}_{eff} under OBCs. For each size L we fit the entanglement profile to Eq. (13) and obtain a single \bar{c}_{eff} subjected

to different measurement intensities and localized potentials, as illustrated in Fig. 4. Near criticality, the half-chain entanglement entropy exhibits logarithmic scaling consistent with non-unitary conformal field theory [125, 126]:

$$\bar{S}(\ell, L) = \frac{\bar{c}_{\text{eff}}}{3} \ln \left[\frac{L}{\pi} \sin \left(\frac{\pi \ell}{L} \right) \right] + s_0, \quad (13)$$

where ℓ is the subsystem size, \bar{c}_{eff} is the effective central charge, and s_0 is a non-universal constant. In the thermodynamic limit, $\bar{c}_{\text{eff}} \rightarrow 0$ in the area-law phase, while it remains finite in the logarithmic phase, thus serving as a diagnostic for the transition [94, 127]. As shown in Fig. 4(a,b), when the localized potential is fixed at a small value ($\Delta = 0.1$ or $V = 0.3$), increasing the measurement strength γ causes \bar{c}_{eff} curves for different system sizes to gradually intersect, indicating a transition near $\gamma \approx 0.3$. The insets strongly corroborate this behavior: as γ increases, the entanglement entropy transitions from rapid growth to saturation, signaling a crossover from log-law to area-law scaling. Similarly, in Fig. 4(c,d), when the measurement strength is fixed at a low value ($\gamma = 0.1$), increasing the localized potential strength leads to similar crossing behavior among different system sizes, with transition points occurring around $\Delta \approx 0.3$ and $V \approx 1.8$, respectively. The insets in Fig. 4 clearly demonstrate this effect: the entanglement entropy drops from steep growth to a nearly constant value as localization increases, again signifying a transition from log-law to area-law behavior. These results collectively indicate that both measurement strength and localized potential can induce a phase transition in the system. In both cases, entanglement growth is suppressed, although the mechanisms and suppression profiles differ between SP and QPP. These observations reveal how both measurement and localization reduce boundary coupling and suppress entanglement growth. The distinct functional behaviors of SP and QPP reinforce the validity of \bar{c}_{eff} as a transition indicator.

Another independent indicator of the entanglement phase transition is the mutual information. As illustrated in Fig. 5(d), the system is partitioned into four segments: subsystems A and B , each occupying $L/8$ sites, are separated by two buffer regions of length $3L/8$. The mutual information is defined as

$$\bar{I}_{A:B} = \bar{S}_A + \bar{S}_B - \bar{S}_{AB}, \quad (14)$$

where \bar{S}_A , \bar{S}_B , and \bar{S}_{AB} denote the entanglement entropies of regions A , B , and $A \cup B$, respectively. Mutual information has proven to be a sensitive diagnostic of MIPT in a variety of systems [40, 54], due to its ability to capture nonlocal correlations. In our study, we adopt the same set of parameters used for computing \bar{c}_{eff} . As shown in Fig. 5(a,b), when the localized potential is set to a small value ($\Delta = 0.1$ or $V = 0.3$), increasing the measurement strength γ leads to a crossing in mutual information curves across different system sizes, signaling the onset of a transition. Similarly, in Fig. 5(c,d), fixing the measurement strength and gradually increasing the potential strength (Δ or V) also induces such crossings, indicative of a phase boundary. To further understand the origin of these

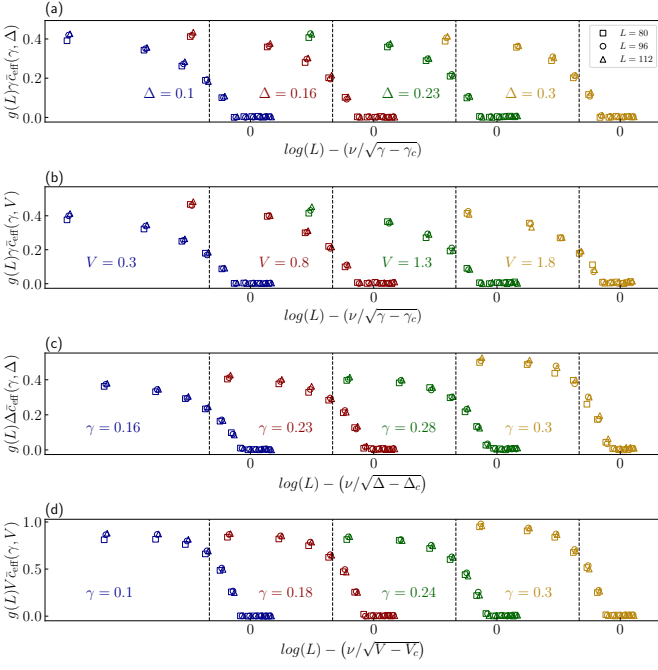


FIG. 6. Finite-size scaling for the effective central charge with the BKT scenario, (a): $g(L)\bar{c}_{\text{eff}}(\gamma, \Delta)$ versus $\log(L) - \nu/\sqrt{\gamma - \gamma_c}$, (b) : $g(L)\bar{c}_{\text{eff}}(\gamma, V)$ versus $\log L - \nu/\sqrt{\gamma - \gamma_c}$. (c): $g(L)\bar{\Delta}_{\text{eff}}(\gamma, \Delta)$ versus $\log(L) - \nu/\sqrt{\Delta - \Delta_c}$, (d): $g(L)\bar{V}_{\text{eff}}(\gamma, V)$ versus $\log L - \nu/\sqrt{V - V_c}$. $g(L) = [1 + 1/(2 \log L - \alpha)]^{-1}$. Detailed numerical data are provided in Table. I.

behaviors, we compute the connected correlation function defined as

$$\bar{C}_\ell = \langle \hat{n}_{L/2} \rangle \langle \hat{n}_{L/2+\ell} \rangle - \langle \hat{n}_{L/2} \hat{n}_{L/2+\ell} \rangle, \quad (15)$$

which reduces to $\bar{C}_\ell = |\langle \hat{c}_{L/2}^\dagger \hat{c}_{L/2+\ell} \rangle|^2$ for the Slater-determinant state $|\psi(t)\rangle$. As shown in the insets of Fig. 5, both increasing measurement strength and localized potential lead to qualitatively similar changes in the correlation structure. In the low measurement or weak localization regime, \bar{C}_ℓ decays algebraically, $\bar{C}_\ell \sim \ell^{-\eta}$, indicating long-range correlations and rapid entanglement growth. In the strong measurement or deep localized regime, \bar{C}_ℓ decays exponentially, $\bar{C}_\ell \sim \exp(-\ell/\xi)$, suggesting short-range correlations and saturation of entanglement entropy consistent with area-law behavior. This sharp decay in the correlation function confirms a transition from an entangled phase with extended quantum coherence to a localized phase dominated by measurement or potential-induced suppression. Together with mutual information crossings, these results demonstrate that both measurement and disorder drive a phase transition that limits entanglement growth, with distinct suppression mechanisms depending on the type of localized potential applied. To quantitatively determine the location and nature of the entanglement phase transition, we perform a finite-size scaling and data collapse analysis of the effective entanglement quantity \bar{c}_{eff} within the Berezinskii-Kosterlitz-Thouless (BKT) framework. Given the pronounced finite-size corrections in free-fermion

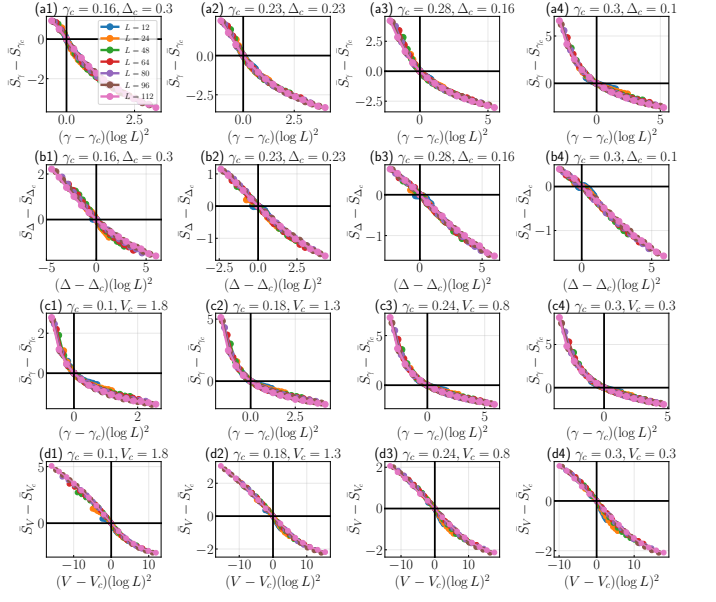


FIG. 7. The finite-size scaling collapse of the entanglement entropy is performed under the assumption of BKT scaling of the correlation length. Subfigures (a) and (b) correspond respectively to the critical points $(\gamma_c, \Delta_c) = (0.16, 0.3), (0.23, 0.23), (0.28, 0.16), (0.30, 0.10)$, where panel (a) is obtained from the collapse of γ data and panel (b) from the collapse of Δ data. Subfigures (c) and (d) correspond respectively to the critical points $(\gamma_c, V_c) = (0.10, 1.8), (0.18, 1.3), (0.24, 1.8), (0.30, 0.3)$, where panel (c) is obtained from the collapse of γ data and panel (d) from the collapse of V data. The analyses are performed using system sizes $L = 12, 24, 48, \dots, 112$.

circuits, simple visual identification of crossing points is unreliable. We adopt a single-parameter scaling ansatz with a mild size correction factor $g(L)$, incorporating the essential singularity of the BKT correlation length, expressed as [94, 128]

$$g(L) x \bar{c}_{\text{eff}}(x, y) = F[\log(L \xi(x, x_c(y)))] \quad (16)$$

where $x \in \{\gamma, \Delta, V\}$ and correlation length $\xi(x, x_c) \sim \exp[-\nu/\sqrt{|x - x_c|}]$. This yields natural scaling variables $X_x = \log L - \nu/\sqrt{|x - x_c|}$ and $Y_x = g(L) x \bar{c}_{\text{eff}}$, allowing us to absorb leading finite-size drift and achieve data collapse onto a unified master curve across system sizes and parameter paths. Fig. 6 illustrates this systematic validation across multiple paths: (a) for fixed localized potential $\Delta = \{0.1, 0.16, 0.23, 0.3\}$, data from system sizes $L = 80, 96, 112$ collapse well after rescaling, enabling precise determination of $\gamma_c(\Delta)$ and a shared ν ; (b) repeating the analysis for different potential strengths $V = \{0.3, 0.8, 1.3, 1.8\}$, we trace the evolution of $\gamma_c(V)$; (c) scanning Δ at fixed measurement strengths $\gamma = \{0.16, 0.23, 0.28, 0.30\}$, we extract $\Delta_c(\gamma)$, which agrees with the inverse function from (a); (d) scanning V at fixed $\gamma = \{0.10, 0.18, 0.24, 0.30\}$, we determine $V_c(\gamma)$, completing the critical boundary in the (γ, V) plane. These appropriate values of γ_c or Δ_c, V_c lead to good scaling collapses, which are consistent with the scaling formula Eq. 16.

TABLE I. Critical exponents and critical points.

Δ	γ_c	ν	α
0.10	0.30 ± 0.035	3.8 ± 0.2	5.9 ± 0.3
0.16	0.28 ± 0.035	4.1 ± 0.2	6.2 ± 0.3
0.23	0.23 ± 0.045	5.7 ± 0.3	6.5 ± 0.45
0.30	0.16 ± 0.040	6.5 ± 0.3	7.3 ± 0.5

V	γ_c	ν	α
0.30	0.30 ± 0.04	2.7 ± 0.3	4.1 ± 0.35
0.80	0.24 ± 0.04	2.9 ± 0.35	4.3 ± 0.35
1.30	0.18 ± 0.04	3.3 ± 0.35	4.5 ± 0.4
1.80	0.10 ± 0.045	3.8 ± 0.4	4.9 ± 0.4

$\gamma(\Delta)$	Δ_c	ν	α
0.16	0.30 ± 0.015	6.5 ± 0.1	8.9 ± 0.1
0.23	0.23 ± 0.03	4.9 ± 0.2	7.4 ± 0.3
0.28	0.16 ± 0.035	4.1 ± 0.3	6.5 ± 0.4
0.30	0.10 ± 0.035	3.3 ± 0.3	4.9 ± 0.4

$\gamma(V)$	V_c	ν	α
0.10	1.8 ± 0.35	3.6 ± 0.35	5.3 ± 0.45
0.18	1.3 ± 0.3	3.2 ± 0.3	4.8 ± 0.45
0.24	0.8 ± 0.15	2.9 ± 0.2	4.1 ± 0.3
0.30	0.1 ± 0.28	2.6 ± 0.3	3.2 ± 0.4

To more precisely determine the phase transition points and to examine whether the transition belongs to the BKT universality class, we perform finite-size scaling analyses for the four critical points using the following scaling relations [128]:

$$\begin{aligned} \bar{S}_\gamma - \bar{S}_{\gamma_c} &= F[(\gamma - \gamma_c)(\log L)^2], \\ \bar{S}_\Delta - \bar{S}_{\Delta_c} &= F[(\Delta - \Delta_c)(\log L)^2], \\ \bar{S}_V - \bar{S}_{V_c} &= F[(V - V_c)(\log L)^2], \end{aligned} \quad (17)$$

where F denotes the scaling function. This scaling formula is based on the assumption that the MIPT belongs to a universality class similar to the BKT one [94], where the correlation length ξ diverges exponentially around the transition point; specifically,

$$\begin{aligned} \log \xi &\sim \frac{1}{\sqrt{\gamma - \gamma_c}} & \text{as } \gamma \rightarrow \gamma_c + 0, \\ \log \xi &\sim \frac{1}{\sqrt{\Delta - \Delta_c}} & \text{as } \Delta \rightarrow \Delta_c + 0, \\ \log \xi &\sim \frac{1}{\sqrt{V - V_c}} & \text{as } V \rightarrow V_c + 0. \end{aligned} \quad (18)$$

As shown in Fig. 7, these transition points yield good scaling collapses, consistent with Eq. 17. The successful scaling collapses provide strong evidence that the phase transition, jointly driven by the measurement strength γ and the Stark potential strength Δ , falls into the BKT universality class. To further determine the error of the phase transition point, we minimize the cost function [57], where the error bar of γ_c or Δ_c , V_c are estimated from the range within which the cost function does not exceed twice their minimum value. The obtained results are presented as circles with error bars in Fig. 2 and are summarized in Table I. The critical points obtained

from all four paths are consistently described using a unified scaling function F and a common critical exponent ν , indicating that the localized potential does not merely shift an isolated critical point but cooperates with measurement strength to generate a continuous phase boundary in the (γ, Δ, V) parameter space. Mathematically, while measurement tends to suppress entanglement, the localized potential restructures the state and alters information transport, and the competition between these effects determines the geometry and location of the phase boundary governed by the BKT singularity. The successful data collapses validate the applicability and robustness of the BKT scaling framework and provide a quantitative foundation for extracting the critical points $\gamma_c(\Delta)$, $\gamma_c(V)$, $\Delta_c(\gamma)$, $V_c(\gamma)$, and the correlation length exponent ν .

IV. CONCLUSION AND DISCUSSION

We investigated the continuous measurement of free fermions under SP and QPP. Our study shows that when the SP strength or the measurement strength is weak, the system remains in a stable logarithmic-scaling phase. Moreover, we found that increasing either the measurement strength or the SP triggers a phase transition, pushing the system into an area-law phase. When the potential strength is strong, we demonstrate that the MIPT disappears, and regardless of the measurement strength, the system remains stable in the area-law phase. To further support these results, we analyzed the central charge, mutual information, and correlation functions. The results reveal that using central charge and mutual information to characterize the system's entanglement behavior clearly exposes a crossover phenomenon, indicating that an increase in either measurement strength or SP leads to an entanglement phase transition. These findings suggest that, qualitatively, Stark localization (caused by SP) and Anderson localization (caused by QPP) play equivalent roles in driving entanglement phase transitions, and both belong to the BKT universality class.

Furthermore, we construct a phase diagram under different localization mechanisms, which diverges at a boundary characterized by entanglement propagation. We find that the monitored Stark-localized system decays rapidly under weak measurement strength, whereas the Anderson-localized system exhibits a slower decay.

Our work highlights the distinctive behavior of MIPTs and relaxation dynamics in Stark-driven monitored systems, and provides a perspective on the characterization of the entanglement phase boundary arising from the combined effects of measurement and localization.

ACKNOWLEDGMENTS

We thank Shuo Liu and Ze-Chuan Liu for the discussions. J.-X. Zhong acknowledges the National Natural Science Foundation of China (Grant No.12374046) and the Shanghai Science and Technology Action Plan (Grant

No.24LZ1400800). H.-Z. Li is supported by the CSC scholarship.

Appendix A: Discussion on the Phase Boundary

As shown in Fig. 8, the entanglement entropy growth of the system exhibits distinct behaviors in different phases. From the figure, in the initial moment ($t \rightarrow 0$) within the Entangling phase the growth obeys:

$$S(t) = G_0 t, \quad (\text{A1})$$

whereas under Critical dynamics it follows:

$$S(t) = C_0 \log(t + 1). \quad (\text{A2})$$

After introducing measurements or localized potentials, the entanglement growth of the system is modified. Denoting the corrections due to measurements and localized potentials by $\Gamma(\gamma)$ and $\Gamma(P)$, respectively, we have:

$$S(t) = \Gamma(\gamma)G_0 t, S(t) = \Gamma(P)G_0 t. \quad (\text{A3})$$

Hence, once measurements and localized potentials suppress the Entangling-phase growth rate down to that of the critical phase, the system reaches criticality:

$$G_0\Gamma(\gamma) + G_0\Gamma(P) = C_0/(t + 1). \quad (\text{A4})$$

For the measurement-induced renormalization of the entanglement-growth rate $\Gamma(\gamma)$, We know that for a continuously monitored fermionic system, the dynamics is governed by the Lindblad master equation:

$$\begin{aligned} \frac{d\rho_t}{dt} &= \mathcal{L}\rho_t \\ &= -i\hat{H}_{\text{eff}}\rho_t + i\rho_t\hat{H}_{\text{eff}}^\dagger + \gamma \sum_m^{L-1} \hat{L}_m \rho_t \hat{L}_m^\dagger, \end{aligned} \quad (\text{A5})$$

where the non-Hermitian effective Hamiltonian H_{eff} is given by Eq. (5). In our actual calculations, we employ the Itô stochastic differential equation averaged over multiple trajectories, so that any amplitude to propagate across L sites without a jump decays as:

$$p_{\text{surv}}(L, t) = e^{-\gamma L t}. \quad (\text{A6})$$

Meanwhile, the unitary Lieb-Robinson bound gives for the creation amplitude across distance L in time t :

$$A_0(L, t) \leq C_0 \exp\left(-\frac{L-vt}{\xi_0}\right). \quad (\text{A7})$$

Requiring both "no-jump" and unitary spread,

$$A(\gamma; L, t) \lesssim C_0 \exp\left(-\frac{L-vt}{\xi_0}\right) \exp(-\gamma L t). \quad (\text{A8})$$

A saddle-point optimization in (L, t) shows that the maximal amplitude obeys:

$$\max_{L, t} A(\gamma; L, t) \propto \exp(-a\gamma^b). \quad (\text{A9})$$

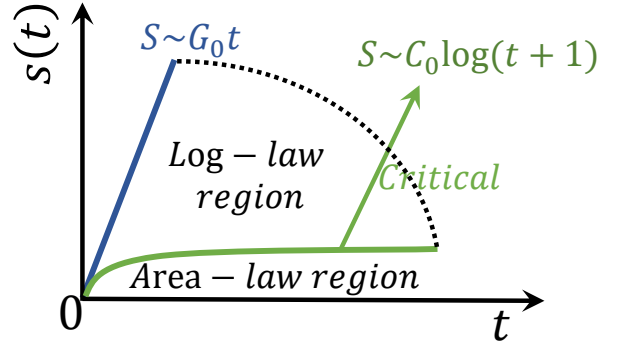


FIG. 8. The growth of bipartite entanglement entropy between the two semi-infinite halves of an infinite chain is shown. In the entangling phase (upper curve) the entanglement grows ballistically with time. At the critical point (middle curve), the entanglement grows logarithmically. In the disentangling phase (lower curve), the entanglement saturates to a finite value.

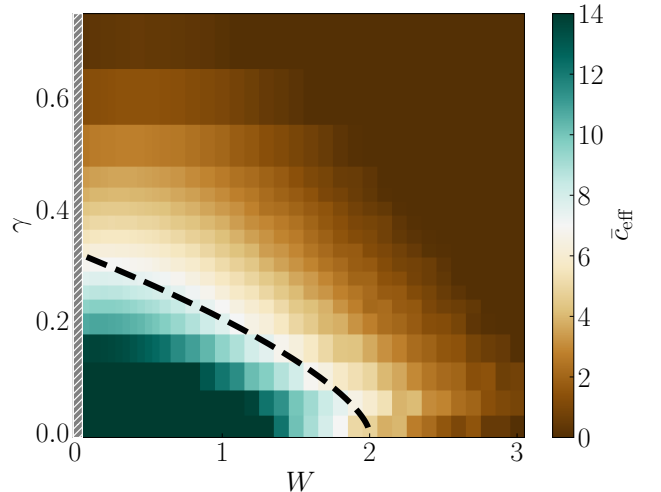


FIG. 9. Phase diagrams and phase boundaries extracted from the effective central charge under joint tuning of the measurement strength and Anderson disorder. Colors indicate the effective central charge \bar{c}_{eff} , extracted from the finite-size scaling of half-chain entanglement entropy: green corresponds to large \bar{c}_{eff} values (log-law-like regime), while brown corresponds to $\bar{c}_{\text{eff}} \rightarrow 0$ (area-law regime). The grey region corresponds to the case of a very weak localization potential, where we tend to revert to the results obtained from the Keldysh field theory [61]. Dashed curves denote the semi-analytical expressions for phase boundaries derived earlier.

Since Γ is proportional to this amplitude scale, we set

$$\Gamma(\gamma) = \exp(-a\gamma^b), \quad (\text{A10})$$

this is the entanglement suppression rate induced by measurement. For the localized potentials induced renormalization of the entanglement-growth rate $\Gamma(P)$, consider the single-particle tight-binding Hamiltonian as shown in Eq. (1), as an

illustrative example, we choose the SP:

$$P_j = F_j, \quad (\text{A11})$$

$F_j = \Delta \cdot j/L$, where Δ denotes the maximum SP. Its eigenstates—the Wannier-Stark ladder—expand in the site basis as:

$$\psi_n(j) = J_{j-n} \left(\frac{2J}{\Delta} \right), \quad (\text{A12})$$

where $J_m(z)$ is the Bessel function. For large order $m \gg z$, one uses the asymptotic

$$J_m(z) \sim \exp(-m \ln \frac{2m}{e z} + O(\ln m)) \quad (\text{A13})$$

$$\approx \exp(-c m^d). \quad (\text{A14})$$

Setting $m \approx |j - n|$ and defining the localization length $\xi = 2J/\Delta$, the effective boundary coupling between regions A and B obeys

$$\|H_{AB}(\Delta)\| = \sum_{i \in A, j \in B} |J_{i-j}(2J/\Delta)| \quad (\text{A15})$$

$$\approx \|H_{AB}\| \exp(-c \Delta^d). \quad (\text{A16})$$

By the same Lieb-Robinson argument, the unitary entanglement growth rate is bounded by:

$$\Gamma(\Delta) \leq \|H_{AB}(\Delta)\|, \quad (\text{A17})$$

and we choose the tight form:

$$\Gamma(\Delta) = G_0 \exp[-c \Delta^d], \quad (\text{A18})$$

this is the entanglement entropy growth rate corrected by the SP. Similarly, for a one-dimensional QPP Eq. (1), the single-particle eigenfunctions localize exponentially with localization length $\xi(V)$. Hence the entanglement entropy growth rate is suppressed to

$$\Gamma(V) = G_0 \exp(-e V). \quad (\text{A19})$$

Then, the phase boundaries in the systems with SP or QPP can be written as:

$$C_0 = \begin{cases} \exp(-a\gamma^b) + \exp(-c \Delta^d), & \text{SP} \\ \exp(-a\gamma^b) + \exp(-e V). & \text{QPP} \end{cases} \quad (\text{A20})$$

Eq. (A20) is the general solution we finally obtain, and in this paper we fix the parameters as $(a, b, c, d, e, C_0) = (6, 1.5, 8, 2, 0.5, 3)$, these parameters are not fundamental physical constants derived analytically, but rather representative values chosen through empirical fitting. The analytical analysis only determines the envelope function form describing the influence of the measurement strength and the localized potential strength on the entanglement growth rate, while the explicit numerical values of the parameters cannot be obtained in closed form. The selected set therefore serves as an effective choice that provides a reasonable description of the numerical phase boundaries and allows us to generate the plots.

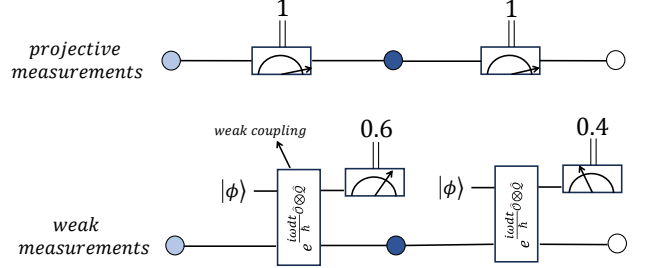


FIG. 10. When a projective measurement is performed on an arbitrary quantum state, the system collapses into an eigenstate of the measurement operator. Consequently, repeated measurements of the same observable will necessarily yield identical outcomes. In contrast, a weak measurement is implemented by weakly coupling the system to an ancillary qubit ϕ , which is then read out. This procedure extracts only partial information about the system without fully projecting it onto an eigenstate. Therefore, a subsequent measurement of the same observable may yield a different outcome and leave the system in a different post-measurement state.

Appendix B: Free fermions with Anderson disorder under measurement

We here complement the results for the SP and QPP by presenting the phase diagram of a one-dimensional chain of free fermions subject to Anderson-type disorder and continuous measurement. We consider spinless free fermions on a one-dimensional lattice with nearest-neighbor hopping J in the presence of uncorrelated on-site disorder as shown in Eq. (1). We set $J = 1$ as the unit of energy and impose the same boundary conditions and filling as in the main text. In the Fig. 9, strong measurement or strong disorder yields an area-law phase with $\bar{c}_{\text{eff}} \approx 0$, while weak measurement and weak disorder produce a logarithmic-entanglement phase with $\bar{c}_{\text{eff}} > 0$. The phase boundary predicted by Eq. (12) in the main text is determined by the competition between the measurement-induced disentangling rate and the effective propagation scale set by localization, and it agrees very well with the numerically obtained transition line. Using the same parameters as for the quasiperiodic potential, we achieve an accurate fit to the phase boundary in the disordered phase diagram. This further supports our conclusion that the phase boundary depends only on the localization characteristics of the wave function; that is, as long as the lattice potential leads to the same degree of localization, the phase boundaries will be similar, largely independent of the specific form of the potential used in the model.

Appendix C: Explanation of the measurement process

We are monitoring the local particle number operator $n_j = c_j^\dagger c_j$ through continuous weak measurement as shown in Fig. 10. Specifically, different from projective measurement,

the core idea of weak measurement is to employ a weak coupling between the system and the measurement apparatus, such that each individual measurement only slightly perturbs the system state while still extracting partial information. To formalize this process, we introduce a continuous measurement outcome x and construct a series of Kraus operators:

$$M(x) = \frac{1}{(2\pi\sigma^2)^{1/4}} e^{-\frac{(x-\omega\hat{O}dt)^2}{4\sigma^2}}, \quad (\text{C1})$$

where, σ describes the width of the probe initial wave function. These operators satisfy the continuous completeness relation $\int dx M^\dagger(x)M(x) = I$. For a single measurement on an initial state $|\psi\rangle$, the probability density of obtaining the result x is given by $p(x) = \langle\psi|M^\dagger(x)M(x)|\psi\rangle$, and the normalized post-measurement state is updated to

$$|\psi(x)\rangle = \frac{M(x)|\psi\rangle}{\sqrt{p(x)}}. \quad (\text{C2})$$

In Kraus representation, to track the evolution of a monitored quantum system at the pure state level and capture the randomness introduced by measurements, one often employs the quantum trajectory method, that is, the Stochastic Schrödinger equation. The evolution of the system over a very short time interval dt is represented by a set of Kraus operators $\{M_\alpha\}$, so that the density matrix evolves as:

$$\rho(t+dt) = \sum_\alpha M_\alpha(dt)\rho(t)M_\alpha^\dagger(dt). \quad (\text{C3})$$

These operators can be divided into two categories:

$$M_0 = I - iH_{\text{eff}}dt, \quad M_k = \sqrt{\gamma dt}L_k. \quad (\text{C4})$$

Here, $H_{\text{eff}} = H - \frac{i\gamma}{2} \sum_{k \geq 1} L_k^\dagger L_k$ is the non-Hermitian effective Hamiltonian and L_k is the jump operator. M_0 and M_k denote the no-jump operator (sometimes referred to as the non-Hermitian evolution operator) and the jump operator, respectively. In the discrete picture, during each small time step dt , the system either evolves without a jump or experiences a single jump. The probability for a jump is determined by a corresponding expression

$$p_{k \geq 1} = \langle\psi(t)|M_k^\dagger M_k|\psi(t)\rangle \approx \gamma dt \langle\psi(t)|L_k^\dagger L_k|\psi(t)\rangle. \quad (\text{C5})$$

If a jump occurs, the state vector is updated according to the jump operator, i.e.,

$$|\psi(t+dt)\rangle = \frac{M_k|\psi(t)\rangle}{\sqrt{p_{k \geq 1}}}, \quad (\text{C6})$$

and if no jump occurs, the state vector evolves under the no-jump operator:

$$|\psi(t+dt)\rangle = \frac{M_0|\psi(t)\rangle}{\sqrt{p_0}}, \quad (\text{C7})$$

where $p_0 = 1 - \sum_{k \geq 1} p_k$ is the probability for no jump. This framework effectively captures the stochastic nature of the evolution in a monitored quantum system.

In the continuous limit $dt \rightarrow 0$, the evolution process can be described by an Itô stochastic differential equation. One of the most common formulations is known as the quantum jump unraveling. In this approach, the state evolves continuously under a non-Hermitian effective Hamiltonian until a quantum jump occurs. The probability of a jump in an infinitesimal time interval is determined by the jump operator, and when a jump occurs, the state is updated according to that operator. Between jumps, the state follows a deterministic (but non-unitary) evolution. Formally, the quantum jump stochastic Schrödinger equation can be written as

$$d|\psi(t)\rangle = -iH_{\text{eff}}|\psi(t)\rangle dt + \sum_{k \geq 1} \left(\frac{L_k|\psi(t)\rangle}{\|L_k|\psi(t)\rangle\|} - |\psi(t)\rangle \right) dN_k(t), \quad (\text{C8})$$

where $dN_k(t)$ is the set of Poisson stochastic increment, this is the Eq. (II) and the Born rule is indeed encoded in the norm of the jump operators $\|L_k|\psi(t)\rangle\|$. The Poisson increments $dN_k(t)$ stochastically determine whether a jump occurs in the interval dt (in the simulations, we set $dt = 0.05$). The probability for a jump is given by

$$p_k = \langle\psi(t)|L_k^\dagger L_k|\psi(t)\rangle dt = \|L_k|\psi(t)\rangle\|^2 dt, \quad (\text{C9})$$

which is precisely the Born probability. The no-jump probability is $p_0 = 1 - \sum_k p_k$. Thus, the randomness of each trajectory is fully governed by the Born rule, not by any artificial filtering. Physical observables are then obtained by averaging over the full ensemble of trajectories, rather than by keeping only a specific subset.

[1] J. M. Deutsch, Quantum statistical mechanics in a closed system, *Physical Review A* **43**, 2046 (1991).

[2] M. Srednicki, Chaos and quantum thermalization, *Physical Review E* **50**, 888 (1994).

[3] M. Rigol, V. Dunjko, and M. Olshanii, Thermalization and its mechanism for generic isolated quantum systems, *Nature* **452**, 854 (2008).

[4] L. D'Alessio, Y. Kafri, A. Polkovnikov, and M. Rigol, From quantum chaos and eigenstate thermalization to statistical mechanics and thermodynamics, *Advances in Physics* **65**, 239 (2016).

(2016).

[5] H. Kim, T. N. Ikeda, and D. A. Huse, Testing whether all eigenstates obey the eigenstate thermalization hypothesis, *Physical Review E* **90**, 052105 (2014).

[6] B. Misra and E. C. G. Sudarshan, The zeno's paradox in quantum theory, *Journal of Mathematical Physics* **18**, 756 (1977).

[7] W. M. Itano, D. J. Heinzen, J. J. Bollinger, and D. J. Wineland, Quantum zeno effect, *Physical Review A* **41**, 2295 (1990).

[8] P. Facchi and S. Pascazio, Quantum zeno subspaces, *Physical Review Letters* **89**, 080401 (2002).

[9] A. G. Kofman and G. Kurizki, Acceleration of quantum decay processes by frequent observations, *Nature* **405**, 546 (2000).

[10] P. Facchi, H. Nakazato, and S. Pascazio, From the quantum zeno to the inverse quantum zeno effect, *Physical Review Letters* **86**, 2699 (2001).

[11] M. P. Fisher, V. Khemani, A. Nahum, and S. Vijay, Random quantum circuits, *Annual Review of Condensed Matter Physics* **14**, 335–379 (2023).

[12] H.-Z. Li, J.-X. Zhong, and X.-J. Yu, Measurement-induced entanglement phase transition in free fermion systems, *Journal of Physics: Condensed Matter* **37**, 273002 (2025).

[13] S. Liu, M.-R. Li, S.-X. Zhang, and S.-K. Jian, Entanglement structure and information protection in noisy hybrid quantum circuits, *Phys. Rev. Lett.* **132**, 240402 (2024).

[14] S. Liu, M.-R. Li, S.-X. Zhang, S.-K. Jian, and H. Yao, Noise-induced phase transitions in hybrid quantum circuits, *Phys. Rev. B* **110**, 064323 (2024).

[15] W. Wang, S. Liu, J. Li, S.-X. Zhang, and S. Yin, Driven critical dynamics in measurement-induced phase transitions, *arXiv: 2411.06648* (2024).

[16] X.-J. Yu, S. Yang, S. Liu, H.-Q. Lin, and S.-K. Jian, Gapless symmetry-protected topological states in measurement-only circuits, *arXiv: 2501.03851* (2025).

[17] X. Huang, H.-Z. Li, Y.-J. Zhao, S. Liu, and J.-X. Zhong, Quantum feedback induced entanglement relaxation and dynamical phase transition in monitored free fermion chains with a wannier-stark ladder, *Phys. Rev. B* **111**, 184302 (2025).

[18] I. Pohoiko, I. V. Gornyi, and A. D. Mirlin, Measurement-Induced Phase Transition for Free Fermions above One Dimension, *Phys. Rev. Lett.* **132**, 110403 (2024).

[19] M. P. Fisher, V. Khemani, A. Nahum, and S. Vijay, Random quantum circuits, *Annual Review of Condensed Matter Physics* **14**, 335 (2023).

[20] Y. Han and X. Chen, Measurement-induced criticality in \mathbb{Z}_2 -symmetric quantum automaton circuits, *Physical Review B* **105**, 064306 (2022).

[21] X. Turkeshi, A. Biella, R. Fazio, M. Dalmonte, and M. Schirò, Measurement-induced entanglement transitions in the quantum ising chain: From infinite to zero clicks, *Physical Review B* **103**, 224210 (2021).

[22] P. Sierant, G. Chiriacò, F. Surace, S. Sharma, X. Turkeshi, M. Dalmonte, R. Fazio, and G. Pagano, Dissipative floquet dynamics: from steady state to measurement induced criticality in trapped-ion chains, *Quantum* **6**, 638 (2022).

[23] P. Sierant and X. Turkeshi, Universal behavior beyond multifractality of wave functions at measurement-induced phase transitions, *Physical Review Letters* **128**, 130605 (2022).

[24] S. Sharma, X. Turkeshi, R. Fazio, and M. Dalmonte, Measurement-induced criticality in extended and long-range unitary circuits, *SciPost Physics Core* **5**, 023 (2022).

[25] X. Turkeshi, Measurement-induced criticality as a data-structure transition, *Physical Review B* **106**, 144313 (2022).

[26] P. Sierant, M. Schirò, M. Lewenstein, and X. Turkeshi, Measurement-induced phase transitions in (d+1)-dimensional stabilizer circuits, *Physical Review B* **106**, 214316 (2022).

[27] A. Pavigliani, X. Turkeshi, M. Schirò, and A. Silva, Enhanced entanglement in the measurement-altered quantum ising chain, *Quantum* **8**, 1576 (2024).

[28] B. Ladewig, S. Diehl, and M. Buchhold, Monitored open fermion dynamics: Exploring the interplay of measurement, decoherence, and free hamiltonian evolution, *Physical Review Research* **4**, 033001 (2022).

[29] M. Buchhold, T. Müller, and S. Diehl, Revealing measurement-induced phase transitions by pre-selection, *arXiv preprint* (2022), 2208.10506.

[30] T. Botzung, M. Buchhold, S. Diehl, and M. Müller, Robustness and measurement-induced percolation of the surface code, *arXiv preprint* (2023), 2311.14338.

[31] W. Wang, S. Liu, J. Li, S. Zhang, and S. Yin, *arxiv:2411.06648*, *arXiv preprint* (2024), 2411.06648.

[32] Z. Xiao, T. Ohtsuki, and K. Kawabata, *arxiv:2408.16974*, *arXiv preprint* (2025), 2408.16974.

[33] T. Jin and D. Martin, Kardar-parisi-zhang physics and phase transition in a classical single random walker under continuous measurement, *Physical Review Letters* **129**, 260603 (2022).

[34] T. Jin and D. Martin, Measurement-induced phase transition in a single-body tight-binding model, *Physical Review B* **110**, L060202 (2024).

[35] G. Lee, T. Jin, Y. Wang, A. McDonald, and A. Clerk, Entanglement phase transition due to reciprocity breaking without measurement or postselection, *PRX Quantum* **5**, 010313 (2024).

[36] M. Adani, S. Cavazzoni, B. Teklu, P. Bordone, and M. Paris, Measurement-induced entanglement phase transition in free fermion systems, *Scientific Reports* **14**, 19933 (2024).

[37] Y. Li, X. Chen, and M. P. A. Fisher, Quantum zeno effect and the many-body entanglement transition, *Physical Review B* **98**, 205136 (2018).

[38] A. Chan, R. M. Nandkishore, M. Pretko, and G. Smith, Unitary-projective entanglement dynamics, *Physical Review B* **99**, 224307 (2019).

[39] B. Skinner, J. Ruhman, and A. Nahum, Measurement-induced phase transitions in the dynamics of entanglement, *Physical Review X* **9**, 031009 (2019).

[40] Y. Li, X. Chen, and M. P. A. Fisher, Measurement-driven entanglement transition in hybrid quantum circuits, *Physical Review B* **100**, 134306 (2019).

[41] M. J. Gullans and D. A. Huse, Dynamical purification phase transition induced by quantum measurements, *Physical Review X* **10**, 041020 (2020).

[42] M. J. Gullans and D. A. Huse, Scalable probes of measurement-induced criticality, *Physical Review Letters* **125**, 070606 (2020).

[43] C.-M. Jian, Y.-Z. You, R. Vasseur, and A. W. W. Ludwig, Measurement-induced criticality in random quantum circuits, *Physical Review B* **101**, 104302 (2020).

[44] Y. Bao, S. Choi, and E. Altman, Theory of the phase transition in random unitary circuits with measurements, *Physical Review B* **101**, 104301 (2020).

[45] S. Choi, Y. Bao, X.-L. Qi, and E. Altman, Quantum error correction in scrambling dynamics and measurement-induced phase transition, *Physical Review Letters* **125**, 030505 (2020).

[46] M. Szyniszewski, A. Romito, and H. Schomerus, Entanglement transition from variable-strength weak measurements, *Physical Review B* **100**, 064204 (2019).

[47] R. Fan, S. Vijay, A. Vishwanath, and Y.-Z. You, Self-organized error correction in random unitary circuits with measurement, *Physical Review B* **103**, 174309 (2021).

[48] S. Vijay, Measurement-driven phase transition within a volume-law entangled phase, arXiv preprint arXiv:2005.03052 (2020), [arXiv:2005.03052 \[quant-ph\]](#).

[49] A. Lavasani, Y. Alavirad, and M. Barkeshli, Measurement-induced topological entanglement transitions in symmetric random quantum circuits, *Nature Physics* **17**, 342 (2021).

[50] S. Sang and T. H. Hsieh, Measurement-protected quantum phases, *Physical Review Research* **3**, 023200 (2021).

[51] M. Ippoliti, M. J. Gullans, S. Gopalakrishnan, D. A. Huse, and V. Khemani, Entanglement phase transitions in measurement-only dynamics, *Physical Review X* **11**, 011030 (2021).

[52] Q. Tang and W. Zhu, Measurement-induced phase transition: A case study in the nonintegrable model by density-matrix renormalization group calculations, *Physical Review Research* **2**, 013022 (2020).

[53] S. Goto and I. Danshita, Measurement-induced transitions of the entanglement scaling law in ultracold gases with controllable dissipation, *Physical Review A* **102**, 033316 (2020).

[54] Y. Fuji and Y. Ashida, Measurement-induced quantum criticality under continuous monitoring, *Physical Review B* **102**, 054302 (2020).

[55] D. Rossini and E. Vicari, Measurement-induced dynamics of many-body systems at quantum criticality, *Physical Review B* **102**, 035119 (2020).

[56] O. Lunt and A. Pal, Measurement-induced entanglement transitions in many-body localized systems, *Physical Review Research* **2**, 043072 (2020).

[57] M. Szyniszewski, O. Lunt, and A. Pal, Disordered monitored free fermions, *Phys. Rev. B* **108**, 165126 (2023).

[58] T. Matsubara, K. Yamamoto, and A. Koga, Measurement-induced phase transitions for free fermions in a quasiperiodic potential, *Phys. Rev. B* **112**, 054309 (2025).

[59] U. Agrawal, A. Zabalo, K. Chen, J. H. Wilson, A. C. Potter, J. H. Pixley, S. Gopalakrishnan, and R. Vasseur, Entanglement and charge-sharpening transitions in U(1) symmetric monitored quantum circuits, *Physical Review X* **12**, 041002 (2022).

[60] F. Barratt, U. Agrawal, S. Gopalakrishnan, D. A. Huse, R. Vasseur, and A. C. Potter, Field theory of charge sharpening in symmetric monitored quantum circuits, *Physical Review Letters* **129**, 120604 (2022).

[61] I. Poboiko, P. Pöpperl, I. V. Gornyi, and A. D. Mirlin, Theory of free fermions under random projective measurements, *Phys. Rev. X* **13**, 041046 (2023).

[62] N. Lang and H. P. Büchler, Entanglement transition in the projective transverse field ising model, *Physical Review B* **102**, 094204 (2020).

[63] M. Coppola, E. Tirrito, D. Karevski, and M. Collura, Growth of entanglement entropy under local projective measurements, *Physical Review B* **105**, 094303 (2022).

[64] M. Szyniszewski, A. Romito, and H. Schomerus, Universality of entanglement transitions from stroboscopic to continuous measurements, *Physical Review Letters* **125**, 210602 (2020).

[65] G. De Tomasi and I. M. Khaymovich, Stable many-body localization under random continuous measurements in the no-click limit, *Physical Review B* **109**, 174205 (2024).

[66] Q. Yang, Y. Zuo, and D. E. Liu, Keldysh nonlinear sigma model for a free-fermion gas under continuous measurements, *Physical Review Research* **5**, 033174 (2023).

[67] H.-Z. Li, X.-J. Yu, and J.-X. Zhong, Non-hermitian stark many-body localization, *Phys. Rev. A* **108**, 043301 (2023).

[68] S. Liu, S.-X. Zhang, C.-Y. Hsieh, S. Zhang, and H. Yao, Discrete time crystal enabled by stark many-body localization, *Phys. Rev. Lett.* **130**, 120403 (2023).

[69] Y.-J. Zhao, H.-Z. Li, X. Huang, S.-Z. Li, and J.-X. Zhong, Fate of pseudomobility edges and multiple states in a non-hermitian wannier-stark lattice, *Phys. Rev. B* **111**, 014315 (2025).

[70] P. W. Anderson, Absence of diffusion in certain random lattices, *Physical Review* **109**, 1492 (1958).

[71] D. J. Thouless, A relation between the density of states and range of localization for one dimensional random systems, *Journal of Physics C: Solid State Physics* **5**, 77 (1972).

[72] E. Abrahams, P. W. Anderson, D. C. Licciardello, and T. V. Ramakrishnan, Scaling theory of localization: Absence of quantum diffusion in two dimensions, *Physical Review Letters* **42**, 673 (1979).

[73] G. H. Wannier, Wave functions and effective hamiltonian for bloch electrons in an electric field, *Physical Review* **117**, 432 (1960).

[74] M. Glück, A. R. Kolovsky, and H. J. Korsch, Wannier-stark resonances in optical and semiconductor superlattices, *Physics Reports* **366**, 103 (2002).

[75] J. X. Zhong and R. Mosseri, Quantum dynamics in quasiperiodic systems, *Journal of Physics: Condensed Matter* **7**, 8383 (1995).

[76] J. Zhong, R. B. Diener, D. A. Steck, W. H. Oskay, M. G. Raizen, E. W. Plummer, Z. Zhang, and Q. Niu, Shape of the quantum diffusion front, *Physical Review Letters* **86**, 2485 (2001).

[77] D. N. Maksimov, E. N. Bulgakov, and A. R. Kolovsky, Wannier-stark states in double-periodic lattices. i. one-dimensional lattices, *Physical Review A* **91**, 053631 (2015).

[78] S. Longhi, Bloch oscillations in complex crystals with pt symmetry, *Physical Review Letters* **103**, 123601 (2009).

[79] L. Bürkle, F. Fuchs, E. Ahlsweide, W. Pletschen, and J. Schmitz, Wannier-stark localization in inas/(gain)sb superlattice diodes, *Physical Review B* **64**, 045315 (2001).

[80] T. Hartmann, F. Keck, H. J. Korsch, and S. Mossmann, Dynamics of bloch oscillations, *New Journal of Physics* **6**, 2 (2004).

[81] H. Z. Li, M. Wan, and J. X. Zhong, Fate of non-hermitian free fermions with wannier-stark ladder, *Physical Review B* **110**, 094310 (2024).

[82] Y. J. Zhao, H. Z. Li, X. Huang, S. Z. Li, and J. X. Zhong, Fate of pseudomobility edges and multiple states in a non-hermitian wannier-stark lattice, *Physical Review B* **111**, 014315 (2025).

[83] X. Huang, H. Z. Li, Y. J. Zhao, S. Liu, and J. X. Zhong, Quantum feedback induced entanglement relaxation and dynamical phase transition in monitored free fermion chains with a wannier-stark ladder, *Physical Review B* **111**, 184302 (2025).

[84] J. E. Lye, L. Fallani, C. Fort, V. Guarrera, M. Modugno, D. S. Wiersma, and M. Inguscio, Effect of interactions on the localization of a bose-einstein condensate in a quasiperiodic lattice, *Physical Review A* **75**, 061603 (2007).

[85] G. Roati, C. D'Errico, L. Fallani, M. Fattori, C. Fort, M. Zaccanti, G. Modugno, M. Modugno, and M. Inguscio, Anderson localization of a non-interacting bose-einstein condensate, *Nature* **453**, 895 (2008).

[86] C. D'Errico, E. Lucioni, L. Tanzi, L. Gori, G. Roux, I. P. McCulloch, T. Giamarchi, M. Inguscio, and G. Modugno, Observation of a disordered bosonic insulator from weak to strong interactions, *Physical Review Letters* **113**, 095301 (2014).

[87] M. Schreiber, S. S. Hodgman, P. Bordia, H. P. Lüschen, M. H. Fischer, R. Vosk, E. Altman, U. Schneider, and I. Bloch, Observation of many-body localization of interacting fermions in a quasirandom optical lattice, *Science* **349**, 842 (2015).

[88] P. Bordia, H. Lüschen, S. Scherg, S. Gopalakrishnan, M. Knap, U. Schneider, and I. Bloch, Probing slow relaxation and many-body localization in two-dimensional quasiperiodic systems, *Physical Review X* **7**, 041047 (2017).

[89] F. A. An, K. Padavić, E. J. Meier, S. Hegde, S. Ganeshan, J. H. Pixley, S. Vishveshwara, and B. Gadway, Interactions and mobility edges: Observing the generalized aubry-andré model, *Physical Review Letters* **126**, 040603 (2021).

[90] P. G. Harper, Single band motion of conduction electrons in a uniform magnetic field, *Proceedings of the Physical Society. Section A* **68**, 874 (1955).

[91] S. Aubry and G. André, Analyticity breaking and anderson localization in incommensurate lattices, *Annals of the Israel Physical Society* **3**, 18 (1980).

[92] T. A. Corcovilos and J. Mittal, Two-dimensional optical quasicrystal potentials for ultracold atom experiments, *Applied Optics* **58**, 2256 (2019).

[93] S. Diehl, A. Micheli, A. Kantian, B. Kraus, H. P. Büchler, and P. Zoller, Quantum states and phases in driven open quantum systems with cold atoms, *Nature Physics* **4**, 878 (2008).

[94] O. Alberton, M. Buchhold, and S. Diehl, Entanglement transition in a monitored free-fermion chain: From extended criticality to area law, *Physical Review Letters* **126**, 170602 (2021).

[95] C. Noel, P. Niroula, D. Zhu, A. Risinger, L. Egan, D. Biswas, M. Cetina, A. V. Gorshkov, M. J. Gullans, D. A. Huse, and C. Monroe, Measurement-induced quantum phases realized in a trapped-ion quantum computer, *Nature Physics* **18**, 760 (2022).

[96] U. Agrawal, J. Lopez-Piqueres, R. Vasseur, S. Gopalakrishnan, and A. C. Potter, Observing quantum measurement collapse as a learnability phase transition, *Physical Review X* **14**, 041012 (2024).

[97] C. W. Kim, J. M. Nichol, A. N. Jordan, and I. Franco, Analog quantum simulation of the dynamics of open quantum systems with quantum dots and microelectronic circuits, *PRX Quantum* **3**, 040308 (2022).

[98] A. J. Daley, Quantum trajectories and open many-body quantum systems, *Advances in Physics* **63**, 77 (2014).

[99] J. Dalibard, Y. Castin, and K. Mølmer, Wave-function approach to dissipative processes in quantum optics, *Physical Review Letters* **68**, 580 (1992).

[100] H. M. Wiseman and G. J. Milburn, Interpretation of quantum jump and diffusion processes illustrated on the bloch sphere, *Physical Review A* **47**, 1652 (1993).

[101] K. Yamamoto and R. Hamazaki, Measurement-induced crossover of quantum jump statistics in postselection-free many-body dynamics (2025), [arXiv:2503.02418 \[cond-mat.stat-mech\]](https://arxiv.org/abs/2503.02418).

[102] In our model with conserved particle number and uniform monitoring, the measurement outcome of $n_j = 0$ is implicitly integrated into the no-jump evolution paths, which simplify to pure unitary dynamics. The measurement outcome of $n_j = 1$ is explicitly expressed in the equation.

[103] H. M. Wiseman and G. J. Milburn, *Quantum Measurement and Control* (Cambridge University Press, Cambridge, 2009).

[104] K. Van Acoleyen, M. Mariën, and F. Verstraete, Entanglement rates and area laws, *Physical Review Letters* **111**, 170501 (2013).

[105] C. H. Bennett, A. W. Harrow, D. W. Leung, and J. A. Smolin, On the capacities of bipartite hamiltonians and unitary gates, *IEEE Transactions on Information Theory* **49**, 1895 (2003).

[106] S. Bravyi, Upper bounds on entangling rates of bipartite hamiltonians, *Physical Review A* **76**, 052319 (2007).

[107] T. Minato, K. Sugimoto, T. Kuwahara, and K. Saito, Fate of measurement-induced phase transition in long-range interactions, *Physical Review Letters* **128**, 010603 (2022).

[108] M. Yang and C. H. Lee, Reversing non-hermitian skin accumulation with a non-local transverse switch, arXiv preprint [arXiv:2509.02686](https://arxiv.org/abs/2509.02686) [10.48550/arXiv.2509.02686](https://doi.org/10.48550/arXiv.2509.02686) (2025).

[109] M. Yang and C. H. Lee, Beyond symmetry protection: Robust feedback-enforced edge states in non-hermitian stacked quantum spin hall systems, arXiv preprint [arXiv:2507.17295](https://arxiv.org/abs/2507.17295) [10.48550/arXiv.2507.17295](https://doi.org/10.48550/arXiv.2507.17295) (2025).

[110] S. Liu, H. Jiang, W.-T. Xue, Q. Li, J. Gong, X. Liu, and C. H. Lee, Non-hermitian entanglement dip from scaling-induced exceptional criticality, arXiv preprint [arXiv:2408.02736](https://arxiv.org/abs/2408.02736) [10.48550/arXiv.2408.02736](https://doi.org/10.48550/arXiv.2408.02736) (2024).

[111] Y. Qin, Y. S. Ang, C. H. Lee, and L. Li, Many-body critical non-hermitian skin effect, arXiv preprint [arXiv:2506.01383](https://arxiv.org/abs/2506.01383) [10.48550/arXiv.2506.01383](https://doi.org/10.48550/arXiv.2506.01383) (2025).

[112] J. M. Koh, W.-T. Xue, T. Tai, D. E. Koh, and C. H. Lee, Interacting non-hermitian edge and cluster bursts on a digital quantum processor, arXiv preprint [arXiv:2503.14595](https://arxiv.org/abs/2503.14595) [10.48550/arXiv.2503.14595](https://doi.org/10.48550/arXiv.2503.14595) (2025).

[113] R. Shen, W. J. Chan, and C. H. Lee, Non-hermitian skin effect along hyperbolic geodesics, *Phys. Rev. B* **111**, 045420 (2025).

[114] S. Yao and Z. Wang, Edge states and topological invariants of non-hermitian systems, *Phys. Rev. Lett.* **121**, 086803 (2018).

[115] S. Yao, F. Song, and Z. Wang, Non-hermitian chern bands, *Phys. Rev. Lett.* **121**, 136802 (2018).

[116] F. Song, S. Yao, and Z. Wang, Non-hermitian skin effect and chiral damping in open quantum systems, *Phys. Rev. Lett.* **123**, 170401 (2019).

[117] F. Song, S. Yao, and Z. Wang, Non-hermitian topological invariants in real space, *Phys. Rev. Lett.* **123**, 246801 (2019).

[118] R. Shen, T. Chen, B. Yang, and C. H. Lee, Observation of the non-hermitian skin effect and fermi skin on a digital quantum computer, *Nature Communications* **16**, 1340 (2025).

[119] Y. Qin, C. H. Lee, and L. Li, Dynamical suppression of many-body non-hermitian skin effect in anyonic systems, *Communications Physics* **8**, 18 (2025).

[120] L. Xiao, T. Deng, K. Wang, G. Zhu, Z. W. W. Yi, and P. Xue, Non-hermitian bulk-boundary correspondence in quantum dynamics, *Nature Physics* **16**, 761 (2020).

[121] M. Yang, L. Yuan, and C. H. Lee, Non-hermitian strong bosonic clustering through interaction-induced caging, *Communications Physics* **8**, 388 (2025).

[122] J. H. Bardarson, F. Pollmann, and J. E. Moore, Unbounded growth of entanglement in models of many-body localization, *Physical Review Letters* **109**, 017202 (2012).

[123] B. Kramer and A. MacKinnon, Localization: theory and experiment, *Reports on Progress in Physics* **56**, 1469 (1993).

[124] E. E. Mendez and G. Bastard, Wannier–stark ladders and bloch oscillations in superlattices, *Physics Today* **46**, 34 (1993).

[125] P. Calabrese and J. Cardy, Entanglement entropy and quantum field theory, *Journal of Statistical Mechanics: Theory and Experiment* **2004**, P06002 (2004).

[126] P. Calabrese and J. Cardy, Entanglement entropy and conformal field theory, *Journal of Physics A: Mathematical and Theoretical* **42**, 504005 (2009).

[127] M. Buchhold, Y. Minoguchi, A. Altland, and S. Diehl, Effective theory for the measurement-induced phase transition of dirac fermions, *Physical Review X* **11**, 041004 (2021).

[128] K. Harada and N. Kawashima, Universal jump in the helicity modulus of the two-dimensional quantum xy model, *Physical Review B* **55**, R11949 (1997).